Journal of Solid State Chemistry 184 (2011) 2648–2654

Contents lists available at ScienceDirect

Journal of Solid State Chemistry

journal homepage: www.elsevier.com/locate/jssc

Phase diagram, chemical stability and physical properties of the solid-solution $Ba_4Nb_{2-x}Ta_xO_9$

Matthew T. Dunstan [a,*], Peter D. Southon [a], Cameron J. Kepert [a], James Hester [b], Justin A. Kimpton [c], Chris D. Ling [a]

[a] School of Chemistry, The University of Sydney, Sydney, NSW 2006, Australia
[b] Bragg Institute, ANSTO, PMB 1, Menai 2234, Australia
[c] Australian Synchrotron, 800 Blackburn Road, Clayton, VIC 3168, Australia

ARTICLE INFO

Article history:
Received 6 May 2011
Received in revised form
21 July 2011
Accepted 22 July 2011
Available online 30 July 2011

Keywords:
6H perovskite
Barium oxides
Carbonate decomposition
Reconstructive phase transition
Phase diagram

ABSTRACT

Through the construction of the $Ba_4Nb_{2-x}Ta_xO_9$ phase diagram, it was discovered that the unique high-temperature γ phase is a thermodynamic intermediate between the low-temperature α phase ($Sr_4Ru_2O_9$-type) and a 6H-perovskite. Refined site occupancies for the γ phase across the $Ba_4Nb_{2-x}Ta_xO_9$ solid-solution indicate that Nb preferentially occupies the tetrahedral sites over the octahedral sites in the structure. When annealed in a CO_2-rich atmosphere, all of the phases studied absorb large amounts of CO_2 at high temperatures between $\sim$700 and 1300 K. *In situ* controlled-atmosphere diffraction studies show that this behaviour is linked to the formation of $BaCO_3$ on the surface of the material, accompanied by a $Ba_5(Nb,Ta)_4O_{15}$ impurity phase. *In situ* diffraction in humid atmospheres also confirms that these materials hydrate below $\sim$1273 K, and that this plays a critical role in the various reconstructive phase transitions as well as giving rise to proton conduction.

1. Introduction

Proton-conducting materials have a number of important possible applications, from sensors to batteries and fuel cell components. A very wide range of materials have been considered and developed from sulfonated polymers such as the perfluorosulfonic acid polymer membrane NAFION [1], layered acidic hydrates [2] and various hydrogenated salts [3–5] amongst many others. Solid-state oxides with complex derivatives of the perovskite-type structure, which exhibit high stability under different atmospheric conditions and temperature ranges, have emerged as the most promising class of new conducting materials for solid state fuel cell applications.

The robust structure of perovskites allows a wide variety of solid solutions and dopant atoms to be incorporated, which in turn can lead to a wide range of exhibited physical properties. For example, mixed perovskites can be developed that conduct electrons, protons and ions in the same phase—the key requirement for oxygen sensors, for example [6,7].

In previous work, we characterised the structures and physical properties of $Ba_4Nb_2O_9$ and $Ba_4Ta_2O_9$, finding them to be mixed electronic, oxide ion and proton conductors [8,9]. The two materials share the same low-temperature α structure, which is isomorphic to that of $Sr_4Ru_2O_9$ [10]. This structure can be described as part of a modulated series of phases built of Ba and NbO_3 columns with ordered cation vacancies [11]. However, upon heating in normal atmospheres, they undergo reconstructive phase transitions to completely different structures. At 1473 K, α-$Ba_4Nb_2O_9$ transforms into γ-$Ba_4Nb_2O_9$, a unique structure type with a supercell that is yet to be solved [8], while at 1513 K α-$Ba_4Ta_2O_9$ transforms into a 6H-perovskite [9]. The different types display varying levels of electronic and ionic conductivity characteristics according to AC impedance spectroscopy and thermogravimetric analysis (TGA) measurements. γ-$Ba_4Nb_2O_9$ shows by far the highest combined proton and oxide ion conductivity, while 6H-$Ba_4Ta_2O_9$ shows the highest mass loss (ascribed to dehydration in our original work [9]) on heating from room temperature.

Considering the differing structures and physical properties of the high-temperature forms of $Ba_4Nb_2O_9$ and $Ba_4Ta_2O_9$, we wished to investigate whether the properties of these materials could be optimised by doping Nb into $Ba_4Ta_2O_9$ and/or Ta into $Ba_4Nb_2O_9$. In the α phase, we expected a continuous solid-solution between the two endpoints given their isomorphic structures, but it was not clear what to expect from the phase diagram at high temperatures.

Our original studies suggested that if Ta could be doped into γ-$Ba_4Nb_2O_9$, it could result in a material with the higher proton

* Corresponding author.
E-mail address: m.dunstan@chem.usyd.edu.au (M.T. Dunstan).

0022-4596/$ - see front matter © 2011 Elsevier Inc. All rights reserved.
doi:10.1016/j.jssc.2011.07.036

conduction of γ-$Ba_4Nb_2O_9$ and the higher proton content (hydration) of 6H-$Ba_4Ta_2O_9$. In γ-$Ba_4Nb_2O_9$, $\frac{1}{3}$ of the Nb atoms are in tetrahedral coordination with the remaining $\frac{2}{3}$ in octahedral coordination in face-sharing Nb_2O_9 dimers [8]. The driving force for the difference between the two high-temperature structures may simply be the greater ability of Nb to adopt tetrahedral coordination than Ta. We therefore expected to be able to dope Ta into all of the octahedral sites, leaving Nb in the tetrahedral sites, i.e. γ-$Ba_4Nb_{2/3}Ta_{4/3}O_9$.

The other aspect of this study was to investigate the role of CO_2 in the structures and properties of these phases. Recently, Bezjak et al. [11] published results suggesting that both the α and γ phases of $Ba_4Nb_2O_9$ are hydrated oxycarbonates rather than simply hydrated oxides. By monitoring evolved gases over the mass-loss curves in TGA using mass spectrometry (MS), they reassigned all of the mass losses (except the lowest temperature one) to CO_2 rather than H_2O. From the magnitude of the mass losses they estimated the total water and carbonate content *per* formula unit at room temperature to correspond to α-$Ba_4Nb_2O_{8.8}(CO_3)_{0.20}.0.1H_2O$ and γ-$Ba_4Nb_2O_{8.42}(CO_3)_{0.58}.0.38H_2O$. Considering the significant proton conductivity of these materials, we sought to investigate these results further using *in situ* synchrotron X-ray powder diffraction (S-XRD), neutron powder diffraction (NPD) and controlled-atmosphere TGA. Furthermore, if these materials are indeed oxycarbonates with CO_2 loss/uptake in the temperature range 573–1273 K and in the presence of water vapour, they may have applications for carbon capture in oxyfuel processes [12,13].

2. Experimental methods

Single-phase polycrystalline samples of α-$Ba_4Nb_{2-x}Ta_xO_9$ for $x=0.0$, 0.4, 0.8, 1.0, 1.2, 1.6 and 2.0 were prepared from commercially available $BaCO_3$, Nb_2O_5 and Ta_2O_5 (99.99% purity or greater). Prior to weighing, $BaCO_3$ was dried at 1000 K overnight. Stoichiometric quantities of the starting materials were weighed and then ground in an agate mortar and pestle under ethanol to improve the homogeneity of the samples. Samples were placed in alumina crucibles and annealed for three periods of 12 h at 1273 K, with regrinding between each successive annealing. Room-temperature XRD data were collected on a Panalytical XPert Pro diffractometer using Cu K_α radiation. All phases appeared to be pure on the basis of these data, pending the higher-resolution synchrotron XRD and neutron powder diffraction experiments described below.

The high-temperature phases were prepared directly from the α samples. Approximately half ($\sim$7.5 g) of each sample was annealed for three periods of 12 h each at 1673 K with regrinding between each successive annealing.

High-temperature S-XRD data were collected at the Powder Diffraction (PD) Beamline of the Australian Synchrotron at $\lambda=0.68933$ Å. Samples were placed on a platinum strip and heated in an Anton-Paar HTK-2000 furnace up to 1723 K. Data were collected in 10 or 25 K steps, with 2×2 minute data collection times in air, dynamic vacuum, flowing CO_2 and flowing humid argon (bubbled though water) atmospheres.

NPD data were obtained using the Echidna (high-resolution) powder diffractometer at the OPAL reactor (Lucas Heights, Australia), at $\lambda=2.4395$ Å. Samples were placed in vanadium cans. Variable temperature measurements were taken up to 1723 K using a cylindrical niobium heating element, with data collected over 1 h at each temperature in 25 K steps.

Controlled-atmosphere TGA experiments were conducted using an IGA-002 gravimetric adsorption instrument (Hiden-Isochema, UK). Samples were held in a quartz bucket within a quartz reaction chamber, and the initial weight recorded. The chamber was evacuated over a period of 30 min at the beginning of measurements, before being heated to 1273 K at a ramp rate of 2 K/min and then cooled back to room temperature at the same rate. CO_2 gas was introduced to the chamber and maintained at a constant pressure of 0.5 bar while heating to 1273 K at 2 K/min. The mass change in the sample was monitored over all variable temperature sequences.

3. Results and discussion

3.1. $Ba_4Nb_{2-x}Ta_xO_9$ thermodynamic phase diagram

The phase diagram for the $Ba_4Nb_{2-x}Ta_xO_9$ solid-solution in air at 1 atm is shown in Fig. 1. The low temperature α phase shows a continuous solid-solution, and at sufficiently high temperatures undergoes two reconstructive phase transitions: first to the γ-$Ba_4Nb_2O_9$ structure, then to the 6H-perovskite structure. The first phase transition temperature follows an approximately linear trend from 1473 K for pure $Ba_4Nb_2O_9$ to 1513 K for pure $Ba_4Ta_2O_9$. The second transition follows a different trend: increasing Ta-content decreases the formation temperature for the 6H-perovskite phase. During optimisation of the synthesis of pure 6H-$Ba_4Ta_2O_9$, it was also discovered that this phase decomposes somewhere between 1573 and 1673 K, forming $Ba_5Ta_4O_{15}$ and other poorly crystalline products that were difficult to identify, but which are presumably Ba-rich. Analysis of the S-XRD diffractograms suggests that this occurs across the entire solid-solution. This behaviour was confirmed by NPD analysis.

Additionally, small amounts of impurities including $BaCO_3$, $Ba_5Ta_4O_{15}$ and $Ba_5Nb_4O_{15}$ were observed in the samples from room-temperature, contrasting with our initial analysis of these samples using laboratory XRD. As described in Section 3.2, we have concluded that these materials slowly decompose in air to form $BaCO_3$ and $Ba_5(Nb,Ta)_4O_{15}$, explaining the presence of these impurity phases. Our failure to previously observe the decomposition products could be due to them forming only a thin and poorly crystalline surface layer on the powder crystallites due to the very slow nature of the decomposition and that the fact that the samples were analysed soon after their synthesis. However, the concentration of these impurities is still quite small compared to the other phases, allowing an accurate determination of the phase behaviour of the α, γ and 6H phases.

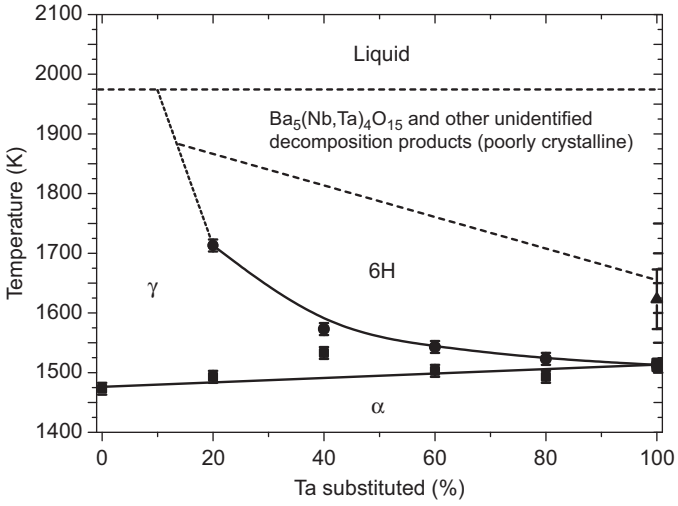

Fig. 1. Thermodynamic phase diagram for the $Ba_4Nb_{2-x}Ta_xO_9$ solid-solution in air. Dotted lines indicate phase boundaries which have been qualitatively (but not quantitatively) defined.

The S-XRD and NPD patterns were used to refine both the low temperature α structure, and (above the phase transition) the γ-$Ba_4Nb_2O_9$ and 6H structures Fig. 2. To perform these refinements we used GSAS with the EXPGUI interface [14,15]. Patterns at 1723 K were refined as a two-phase mixture, and sequential refinements carried out back towards the phase transition. Similarly, α single phases were sequentially refined from 1273 K with increasing temperature.

The refined lattice parameters for all phases were constant within error across the solid-solution, and were essentially unchanged from those of the pure $Ba_4Nb_2O_9$ and $Ba_4Ta_2O_9$ end-members [8,9], as shown in Fig. 3. Considering the identical effective ionic radii of niobium and tantalum (0.64 Å for both [16]), this was to be expected. A representative plot of lattice parameters against temperature for $Ba_4Nb_2O_9$ in air in shown in Fig. 4. Apart from a slight increase in all parameters from thermal expansion, there are no major changes apart from at the reconstructive phase transition at 1473 K.

As an example of the trends in lattice parameters across the solid-solution, a plot of unit cell volume for the phases present with increasing temperature for the four samples in the $Ba_4Nb_{2-x}Ta_xO_9$ series is shown in Fig. 5. There appear to be no clear statistically significant trends besides thermal expansion,

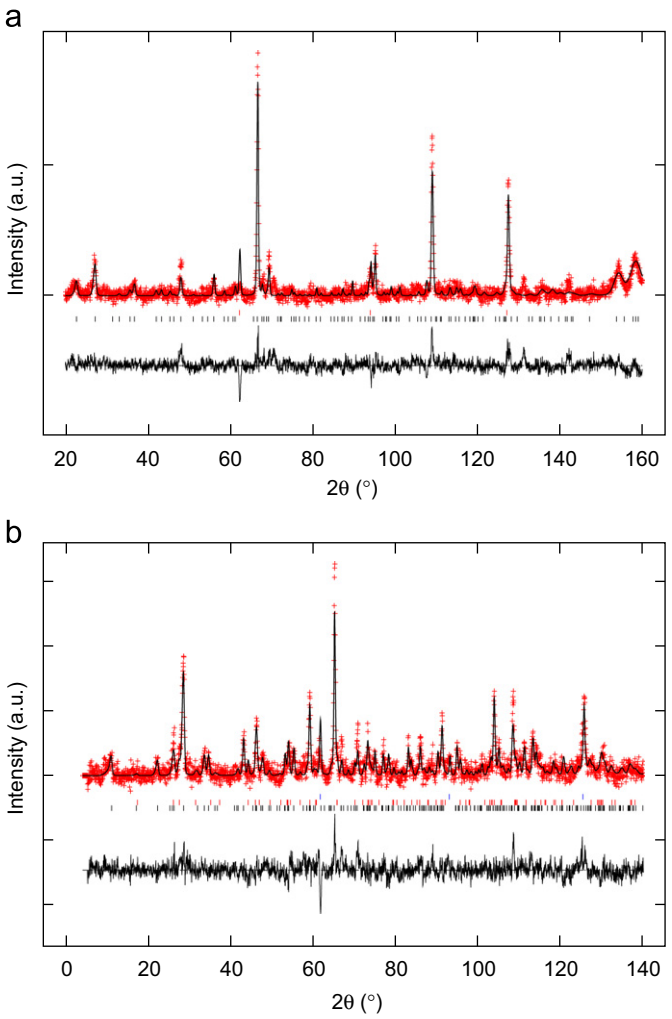

Fig. 2. Rietveld-refinement results for $Ba_4Nb_{1.6}Ta_{0.4}O_9$ against Echidna NPD data ($\lambda = 2.4395$ Å). (a) α phase at 1273 K and (b) a two phase mixture at 1723 K. The first row of peak markers in both diffractograms are for the niobium heating element. For (a), the second row of markers are for the α phase, and for (b) the next two rows are for the γ-$Ba_4Nb_2O_9$ and 6H phases.

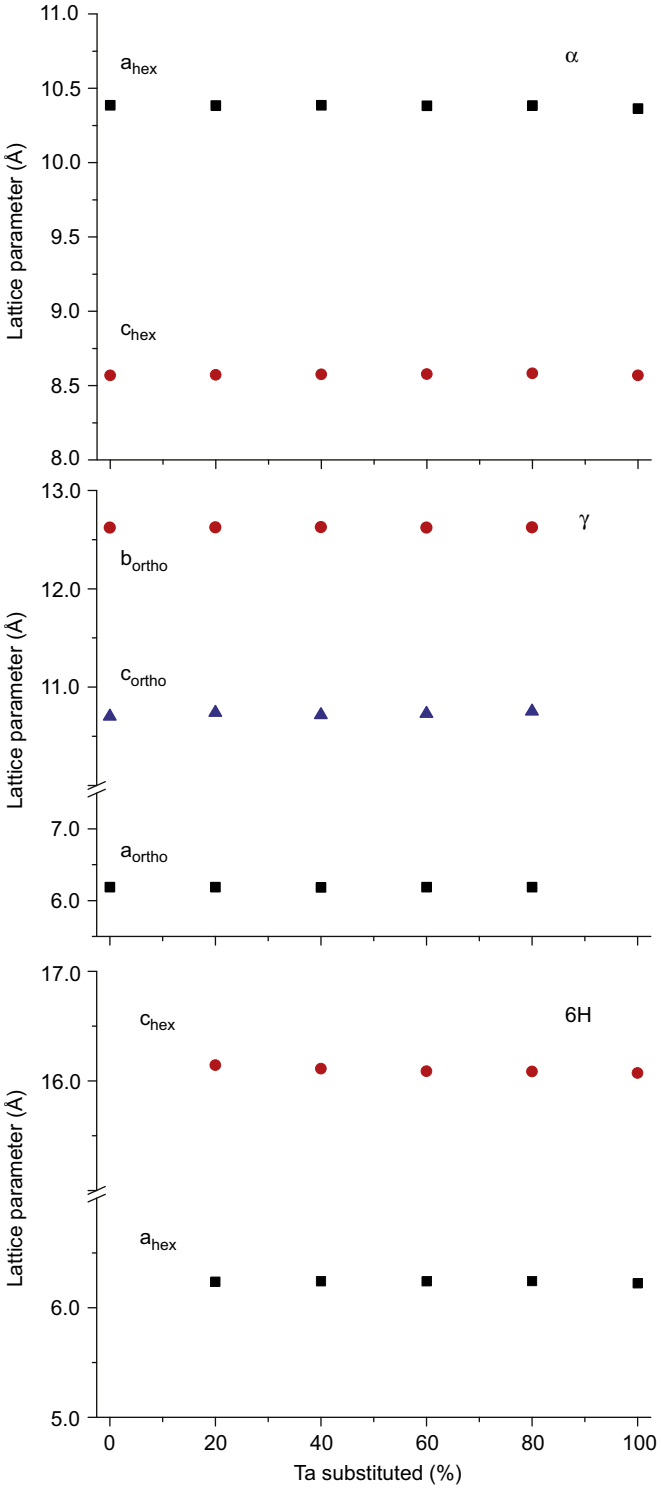

Fig. 3. Rietveld-refined lattice parameters for the three phases across the entire $Ba_4Nb_{2-x}Ta_xO_9$ solid-solution range, obtained from *in situ* NPD. The lattice parameters are compared at constant temperatures across composition: at 1273 K for the α phase, 1523 K for the γ phase and 1723 K for the 6H phase.

and the phases have the same structure regardless of the Nb:Ta ratio. As the phase transitions are reconstructive and kinetically limited, some α phase persists in the diffraction patterns above the phase transition temperature (and similarly for the γ-$Ba_4Nb_2O_9$ phase above its phase transition).

We were able to refine individual occupancies on the 4- and 6-fold coordinate metal sites in γ-$Ba_4Nb_2O_9$ compared to

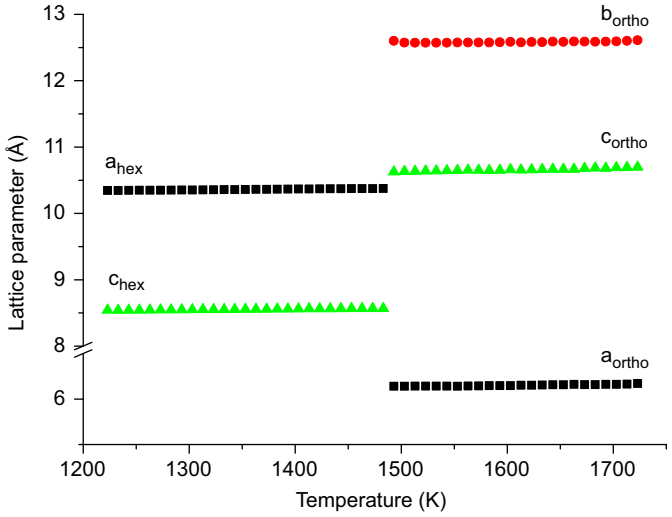

Fig. 4. Rietveld-refined (against synchrotron XRD data) lattice parameters with increasing temperature. The plot shows the change from the hexagonal α phase to orthorhombic γ-$Ba_4Nb_2O_9$ phase.

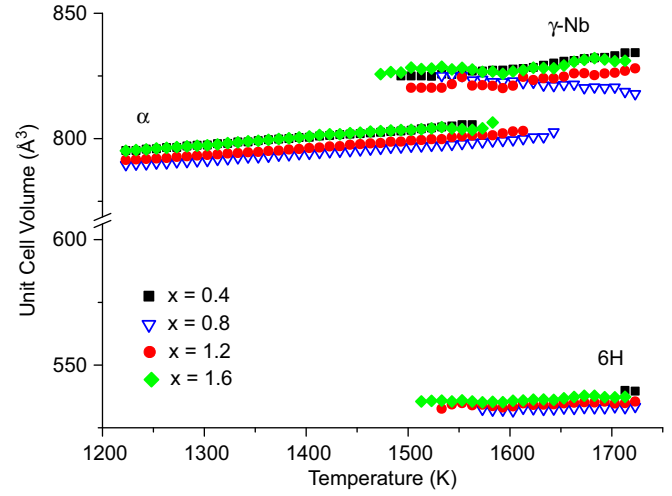

Fig. 5. Rietveld-refined (against synchrotron XRD data) unit cell volume with increasing temperature for the samples in the $Ba_4Nb_{2-x}Ta_xO_9$ series. The plot shows the change from the hexagonal α phases to orthorhombic γ-$Ba_4Nb_2O_9$ and hexagonal 6H-$Ba_4Ta_2O_9$. Due to the kinetically limited nature of the phase transitions, the three phases can coexist and hence the overlap in the refinements.

Table 1
Refined occupancies for both phases of $Ba_4Nb_{0.8}Ta_{1.2}O_9$ at 1723 K.

Phase	Crystallographic site	Occupancy (Nb/Ta)
γ	*M*1 (Octahedral)	0.50(2)/0.50(2)
	*M*2 (Octahedral)	0.34(3)/0.66(3)
	*M*3 (Tetrahedral)	0.89(2)/0.11(2)
6H	*M*1 (Octahedral)	0.50(2)/0.50(2)

6H-$Ba_4Ta_2O_9$, for example in Ba4$Nb_{0.8}Ta_{1.2}$O9 (Table 1). The same trend is present across the whole solid-solution: niobium shows a strong preference for the tetrahedral site in γ-$Ba_4Nb_{2-x}Ta_xO_9$, regardless of the Nb:Ta ratio. This supports our hypothesis that it is the greater ability of niobium atoms to adopt a four-fold coordination which favours the formation of the γ phase over the 6H phase. The higher energy of tantalum atoms in this coordination environment explains why pure α-$Ba_4Ta_2O_9$ shows no γ intermediate.

3.2. Controlled-atmosphere studies

In order to investigate the observations of Bezjak et al. and their suggestion that these materials are oxycarbonates, we performed a variable-temperature *in situ* S-XRD experiment under 1 atm of flowing CO_2. Data for α-$Ba_4Nb_2O_9$ and α-$Ba_4Ta_2O_9$ were obtained in 10 K steps from 1223 to 1723 K. Surprisingly, the phase transition to γ-$Ba_4Nb_2O_9$ was observed at a lower temperature: 1403 K under CO_2 as compared to 1493 K under air. For $Ba_4Ta_2O_9$, we also saw a reduction in its phase transition to 6H-$Ba_4Ta_2O_9$, from 1513 to 1483 K. A second experiment on α-$Ba_4Ta_2O_9$, heated from room temperature to 1223 K under CO_2, shed more light on the role of CO_2. Fig. 6 shows that at 973 K, α-$Ba_4Ta_2O_9$ decomposes to $Ba_5Ta_4O_{15}$ [16] and $BaCO_3$. A second transition, observed at ~1073 K, corresponds to the orthorhombic *Pmcn* → trigonal *R*3*m* transition of $BaCO_3$, reported to occur at 1084 K [17]. The patterns above 973 K were refined using GSAS, with the results shown in Fig. 7.

We investigated this further in CO_2 absorption experiments under vacuum and CO_2 using controlled-atmosphere TGA. The percentage change in sample weight on heating under 0.5 atm CO_2, normalised to the lowest observed mass, is shown in Fig. 8. The black line, showing the behaviour of the sample under vacuum, is very similar to the DTA data of Bezjak et al. for α-$Ba_4Nb_2O_9$. We then see a slight increase in sample weight which quickly stabilises on cooling. On heating under CO_2 from 873 K we see a sharp increase in the sample mass of $>5.5\%$ over ~100 K. This can only be due to the absorption of CO_2. The amount of CO_2 absorbed in this step corresponds to ~1 molecule *per* formula unit, whereas the complete decomposition of α-$Ba_4Ta_2O_9$ should require 1.5 CO_2 *per* formula unit ($3CO_2 + 2Ba_4Ta_2O_9 \rightarrow Ba_5Ta_4O_{15} + 3BaCO_3$). This suggests that a substantial amount of the material had already decomposed in this way, as evidenced by the presence of these impurities in the S-XRD patterns at room-temperature. It also suggests that the lower formation temperatures for both 6H-$Ba_4Ta_2O_9$ and γ-$Ba_4Nb_2O_9$

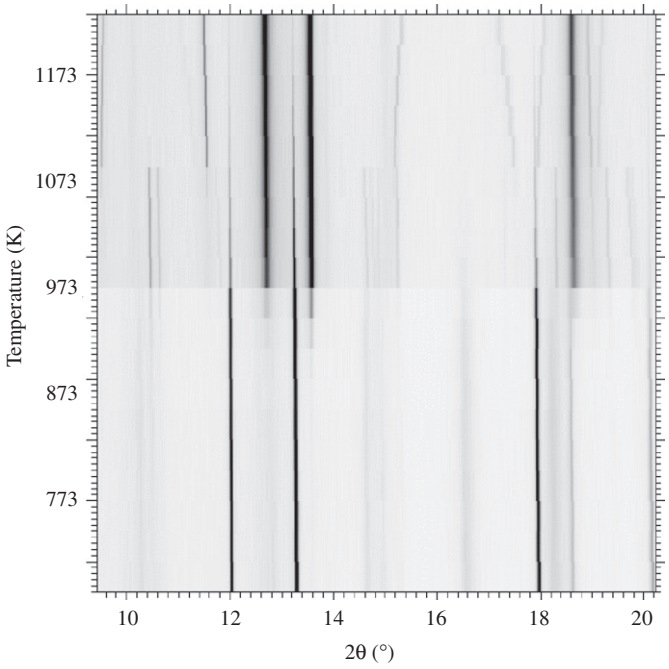

Fig. 6. Part of the S-XRD ($\lambda = 0.68933$ Å) diffractograms of α-$Ba_4Ta_2O_9$ under CO_2 from room temperature to 1223 K. The clear and abrupt decomposition and simultaneous formation of $BaCO_3$ and $Ba_5Ta_4O_{15}$ can be seen at 973 K. The orthorhombic to trigonal transformation of $BaCO_3$ is also observed at 1073 K.

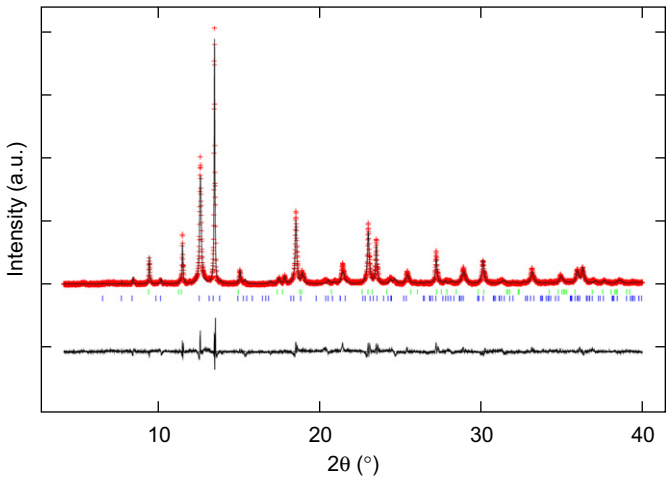

Fig. 7. Rietveld refinement results for α-$Ba_4Ta_2O_9$ after decomposition to $BaCO_3$ and $Ba_5Ta_4O_{15}$, against synchrotron XRD data ($\lambda = 0.68933$ Å) at 1273 K under flowing CO_2. Crosses are observed data, solid line is the calculated fit, and the lower solid line is the difference curve. The first row of peak markers are the $Ba_5Ta_4O_{15}$ phase, and the second row are the high-temperature trigonal $BaCO_3$ phase.

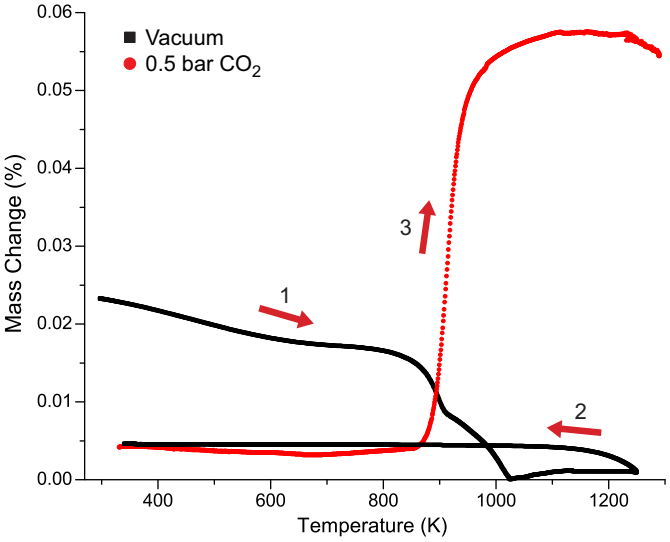

Fig. 8. IGA results for α-$Ba_4Ta_2O_9$ heated (1) and cooled (2) under vacuum and then heated (3) under 0.5 bar CO_2.

under 1 atm CO_2 (*versus* air), seen in our *in situ* S-XRD experiments, is due to less energy being required for their formation from the decomposition products than directly from the α phases.

Controlled-atmosphere TGA curves and refined phase fractions for all four materials are compared in Fig. 9. The phase fractions were obtained from Rietveld refinement against S-XRD data, with samples that were pretreated in the same fashion as for the IGA experiments (heated to 1273 K and cooled under vacuum, and then exposed to CO_2). Refined phases were the nominal compound (α-$Ba_4Nb_2O_9$, α-$Ba_4Ta_2O_9$, γ-$Ba_4Nb_2O_9$ or 6H-$Ba_4Ta_2O_9$), the low and high-temperature phases of $BaCO_3$ and $Ba_5(Ta,Nb)_4O_{15}$ [16]. An exception was the γ-$Ba_4Nb_2O_9$ sample, where it was not possible to accurately refine the γ phase and $BaCO_3$ simultaneously due to significant peak overlap, and therefore only the γ-$Ba_4Nb_2O_9$ and $Ba_5Nb_4O_{15}$ phase fractions are compared.

For all the materials there was S-XRD evidence of $BaCO_3$ in the samples at room temperature even before treatment with CO_2. Considering that the samples were synthesised some weeks prior to analysis and had been exposed to air, this implies that the decomposition process can occur under atmospheric concentrations of CO_2 at room temperature. However, the accompanying decomposition product, $Ba_5(Nb,Ta)_4O_{15}$ was not observed, except in the α-$Ba_4Nb_2O_9$ sample. Interestingly, the α-$Ba_4Nb_2O_9$ sample is also the only one that did not decompose completely by 1273 K. The refined phase fractions show an initial fall in α-$Ba_4Nb_2O_9$ accompanied by an equal rise in $Ba_5Nb_4O_{15}$ at ~925 K. At ~1175 K this is reversed with α-$Ba_4Nb_2O_9$ being regenerated as we approach 1273 K. The α-$Ba_4Nb_2O_9$ sample was synthesised at 1273 K, so these results further support the hypothesis that partial decomposition occurs on cooling from the initial synthesis temperature.

We agree with the conclusions of Bezjak et al. that most of the mass loss seen in the TGA curves is due to the evolution of CO_2, not H_2O as we originally inferred. Concordantly, our inference that the Ta phases hydrated to a greater extent than the Nb phases, especially in a direct comparison of the two α phases [9], was incorrect. These materials have much lower proton concentrations than previously thought, and the strategy of optimising the mixed ionic-electronic conductivity by doping with Ta may not be valid. However, while the first mass loss at ~373 K is almost certainly the loss of surface water, both our observations and those of Bezjak et al. confirm the presence of water in these materials up to 1273 K. While the mole amount is less than we originally reported, hydroxide ions and protons in γ-$Ba_4Nb_2O_9$ (in particular) are still crucial features of these materials and are responsible for its high oxide ion and proton conductivity. This is supported by further *in situ* controlled-atmosphere S-XRD experiments under humid Ar in the absence of CO_2, which showed these conditions promoted the α→γ and α→6H transitions to lower temperatures (1453 and 1443 K, respectively). Furthermore, no structural changes or decomposition products were observed, confirming these materials to be stable in humid atmospheres under high temperatures (up to ~1450 K).

4. Conclusions

The $Ba_4Nb_{2-x}Ta_xO_9$ phase diagram is substantially more complex than expected. Firstly, both the γ and 6H phases are accessible across almost the entire solid-solution, with the γ phase being a thermodynamic intermediate between the α and 6H phases. With careful annealing at temperatures between the α→γ transition and the γ→6H transition, single phases of γ-$Ba_4Nb_{2-x}Ta_xO_9$ can be synthesised right across the solid-solution and quenched to room temperature. For Nb-rich compositions, the stability zone of the γ phase extends to the melting point, precluding the formation of a 6H-type phase. Secondly, Nb preferentially occupies the tetrahedral sites over the octahedral sites in the γ phase, explaining the reduced stability region of the γ phase as x increases.

The ready decomposition of these materials in CO_2-containing atmospheres adequately explains the observations of Bezjak et al. without the need to redefine them as oxycarbonates. Similar decomposition processes have been found for other mixed ionic-electronic conductors under high-CO_2 atmospheres, including a range of barium-based perovskites containing Co, Fe and Nb [18]. In that study it was found that the reactivity (or stability) of a metal oxide with an acidic gas such as CO_2 depends on the metal's relative Lewis acidity. Oxides of metals with higher Lewis acidity were shown to be more resistant to decomposition under CO_2. According to Jeong et al. [19], Nb_2O_5 has a similar Lewis acidity to Ta_2O_5, with a scaling of 3.9 compared to 3.7, reflecting the similar behaviour of the Nb and Ta phases in this study. The slightly higher resistance of Nb oxides to CO_2 could explain the slower mass increase seen in the IGA

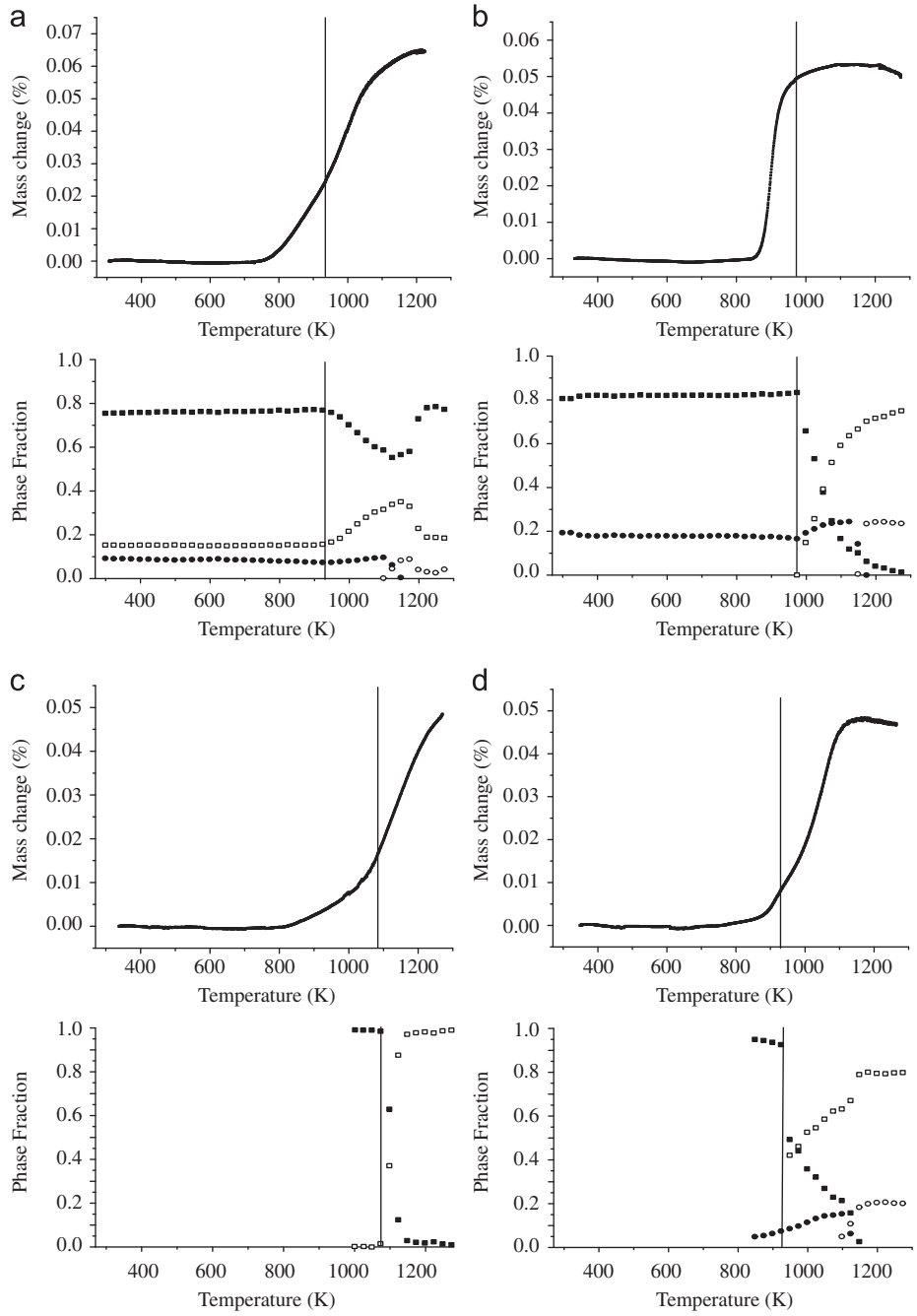

Fig. 9. Mass change and normalised phase fractions for (a) α-$Ba_4Nb_2O_9$, (b) α-$Ba_4Ta_2O_9$, (c) γ-$Ba_4Nb_2O_9$ and (d) 6H-$Ba_4Ta_2O_9$, obtained from heating from room-temperature to 1273 K under CO_2. The original phase in each is shown as black squares, with the decomposition product ($Ba_5Nb_4O_{15}$ or $Ba_5Ta_4O_{15}$) shown in white squares. The other symbols refer to the low-temperature orthorhombic (black circles) and high-temperature trigonal phases (white circles) of $BaCO_3$. The mass change is normalised to the mass at 323 K.

curve for α-$Ba_4Nb_2O_9$ compared to α-$Ba_4Ta_2O_9$. Considering the growing interest in carbon-capture for oxyfuel combustion processes and high-temperature solid-oxide fuel cells [12,13,20], the combination of high oxygen permeation, CO_2 absorption at high temperatures and robustness to humid atmospheres in a single material is unusual. Although decomposition of the nominal phases are an integral part of these processes, the fact that they readily reform on subsequent heating in CO_2-poor atmospheres means that they may well be of practical interest.

Despite the observed partial decomposition to $BaCO_3$ and $Ba_5(Nb,Ta)_4O_{15}$, these materials may still be of interest for mixed electronic, oxide ion and proton conductivity applications at high temperatures and in atmospheres containing high amounts of CO_2. The degradation and formation of surface $BaCO_3$ in other mixed ionic-electronic conducting perovskites has been linked to a dramatic and instantaneous decrease in oxygen permeation flux, rendering them unsuitable for use in CO_2-containing atmospheres [21–23], but our original conductivity results show that these materials retain quite good performance [8,9], even after partial decomposition upon cooling and storage in CO_2-containing atmospheres. This may be because they recover/reform readily on heating above 1500 K.

Acknowledgments

This work was supported by the Australian Research Council—Discovery Projects (No. DP110102662).

References

[1] R. Slade, J. Barker, J. Strange, Solid State Ionics 35 (1989) 11.
[2] V. Linkov, Membr. Technol. 132 (2001) 4.
[3] C.R.I. Chisholm, S.M. Haile, Solid State Ionics 145 (2001) 179.
[4] A.I. Baranov, L.A. Shuvalov, N.M. Shchagina, J. Exp. Theor. Phys. Lett. 36 (1982) 459.
[5] A. Potier, D. Roussele, J. Chim. Phys. Phys.-Chim. Biol. 70 (1973) 873.
[6] J.W. Phair, S.P.S. Badwal, Ionics 12 (2006) 103.
[7] A. Orera, P.R. Slater, Chem. Mater. 22 (2010) 675.
[8] C.D. Ling, M. Avdeev, R. Kutteh, V.V. Kharton, A.A. Yaremchenko, S. Fialkova, N. Sharma, R.B. Macquart, M. Hoelzel, M. Gutmann, Chem. Mater. 21 (2009) 3853.
[9] C.D. Ling, M. Avdeev, V.V. Kharton, A.A. Yaremchenko, R.B. Macquart, M. Hoelzel, Chem. Mater. 22 (2010) 532.
[10] C. Dussarrat, J. Fompeyrine, J. Darriet, Eur. J. Solid State Inorg. Chem. 32 (1995) 3.
[11] J. Bezjak, A.M. Abakumov, A. Recnik, M.M. Krzmanc, B. Jancar, D. Suvorov, J. Solid State Chem. 183 (2010) 1823.
[12] S.U. Park, T.S. Kim, J.L. Sohn, Y.D. Lee, Appl. Energ. 88 (2011) 1187.
[13] P.N. Dyer, R.E. Richards, S.L. Russeka, D.M. Taylor, Solid State Ionics 134 (2000) 21.
[14] A.C. Larson, R.B. von Dreele, GSAS: The General Structure Analysis Program, Los Alamos National Laboratory, Los Alamos, NM, 1990.
[15] B.H. Toby, J. Appl. Cryst. 34 (2001) 210.
[16] J. Shannon, L. Katz, Acta Crystallogr. B 26 (1970) 102.
[17] S.M. Antao, I. Hassan, Phys. Chem. Miner. 34 (2007) 573.
[18] J. Yi, M. Schroeder, T. Weirich, J. Mayer, Chem. Mater. 22 (2010) 6246.
[19] N.C. Jeong, J.S. Lee, E.L. Tae, Y.J. Lee, K.B. Yoon, Angew. Chem. Int. Ed. 47 (2008) 10128.
[20] S. Engels, F. Beggel, M. Modigell, H. Stadler, J. Membr. Sci. 359 (2010) 93.
[21] J.X. Yi, S.J. Feng, Y.B. Zuo, W. Liu, C.S. Chen, Chem. Mater. 17 (2005) 5856.
[22] J.H. Tong, W.S. Yang, B.C. Zhu, R.J. Cai, J. Membr. Sci. 203 (2002) 175.
[23] M. Arnold, H.H. Wang, A. Feldoff, J. Membr. Sci. 294 (2007) 44.